1

# Multimode Nonlinear Fibre Optics: Theory and Applications

Peter Horak and Francesco Poletti
*University of Southampton*
*United Kingdom*

## 1. Introduction

Optical fibres have been developed as an ideal medium for the delivery of optical pulses ever since their inception (Kao & Hockham, 1966). Much of that development has been focused on the transmission of low-energy pulses for communication purposes and thus fibres have been optimised for singlemode guidance with minimum propagation losses only limited by the intrinsic material absorption of silica glass of about 0.2dB/km in the near infrared part of the spectrum (Miya et al., 1979). The corresponding increase in accessible transmission length simultaneously started the interest in nonlinear fibre optics, for example with early work on the stimulated Raman effect (Stolen et al., 1972) and on optical solitons (Hasegawa & Tappert, 1973). Since the advent of fibre amplifiers (Mears et al., 1987), available fibre-coupled laser powers have been increasing dramatically and, in particular, fibre lasers now exceed kW levels in continuous wave (cw) operation (Jeong et al., 2004) and MW peak powers for pulses (Galvanauskas et al., 2007) in all-fibre systems. These developments are pushing the limits of current fibre technology, demanding fibres with larger mode areas and higher damage threshold. However, it is increasingly difficult to meet these requirements with fibres supporting one single optical mode and therefore often multiple modes are guided.

Non-fibre-based laser systems are capable of delivering even larger peak powers, for example commercial Ti:sapphire fs lasers now reach the GW regime. Such extreme powers cannot be transmitted in conventional glass fibres at all without destroying them (Gaeta, 2000), but there is a range of applications for such pulses coupled into hollow-core capillaries, such as pulse compression (Sartania et al., 1997) and high-harmonic generation (Rundquist et al., 1998). For typical experimental parameters, these capillaries act as optical waveguides for a large number of spatial modes and modal interactions contribute significantly to the system dynamics.

In order to design ever more efficient fibre lasers, to optimise pulse delivery and to control nonlinear applications in the high power regime, a thorough understanding of pulse propagation and nonlinear interactions in multimode fibres and waveguides is required. The conventional tools for modelling and investigating such systems are based on beam propagation methods (Okamoto, 2006). However, these are numerically expensive and provide little insight into the dependence of fundamental nonlinear processes on specific fibre properties, e.g., on transverse mode functions, dispersion and nonlinear mode coupling. For such an interpretation a multimode equivalent of the nonlinear Schrödinger equation, the

standard and highly accurate method for describing singlemode nonlinear pulse propagation (Agrawal, 2001; Blow & Wood, 1989), is desirable.
In this chapter, we discuss the basics of such a multimode generalised nonlinear Schrödinger equation (Poletti & Horak, 2008), its simplification to experimentally relevant situations and a few select applications. We start by introducing and discussing the theoretical framework for fibres with $\chi^{(3)}$ nonlinearity in Sec. 2. The following sections are devoted to multimode nonlinear applications, presented in the order of increasing laser peak powers. A sample application in the multi-kW regime is supercontinuum generation, discussed in Sec. 3. Here we demonstrate how fibre mode symmetries and launching conditions affect intermodal power transfer and spectral broadening. For peak powers in the MW regime, self-focusing effects become significant and lead to strong mode coupling. The spatio-temporal evolution of pulses in this limit is the topic of Sec. 4. Finally, at GW peak power levels, optical pulses can only be delivered by propagation in gases. Still, intensities become so high that nonlinear effects related to ionisation must be taken into account. An extension of the multimode theory to include these extreme high power effects is presented in Sec. 5 and the significance of mode interaction is demonstrated by numerical examples pertaining to a recent experiment. Finally, we end this chapter with conclusions in Sec. 6.

## 2. The multimode generalised nonlinear Schrödinger equation

Pulse propagation in singlemode fibres is frequently modelled by a generalised nonlinear Schrödinger equation (NLSE) which describes the evolution of the electric field amplitude envelope of an optical pulse as it propagates along the fibre (Agrawal, 2001; Blow & Wood, 1989). This framework has been extremely successful in incorporating all linear and nonlinear effects usually encountered in fibres, such as second and higher order dispersion, Kerr and Raman nonlinearities and self-steepening, and its predictions have been corroborated by numerous experiments using conventional fibres, photonic crystal fibres and fibre tapers of different materials, as well as laser sources from the continuous wave regime down to few cycle pulses. Perhaps the most prominent application of the NLSE is in the description of supercontinuum generation where all the linear and nonlinear dispersion effects come together to induce spectacular spectral broadening of light, often over very short propagation distances (Dudley et al., 2006).
For very high power applications, as motivated above, a further extension of the NLSE is required to deal with the multimode aspects of large-mode area fibres. A very general multimode framework has been presented recently allowing for arbitrary mode numbers, polarisations, tight mode confinements and ultrashort pulses (Poletti & Horak, 2008). Here we describe a slightly simplified version that is more easily tractable and still is applicable to many realistic situations, e.g., for the description of high power applications as discussed in the later sections.
We start by considering a laser pulse propagating in a multimode fibre. The pulse can be written as the product of a carrier wave $\exp[i(\beta_0^{(0)} z - \omega_0 t)]$, where $\omega_0$ is the carrier angular frequency and $\beta_0^{(0)}$ is its propagation constant in the fundamental fibre mode, and an envelope function $\mathbf{E}(\mathbf{x}, t)$ in space and time. Note that throughout this chapter we adopt the notation that vectorial quantities are written in bold face and $\mathbf{x} = (x, y, z)$. For convenience, we assume $\mathbf{E}(\mathbf{x}, t)$ to be complex-valued, so that it includes the envelope phase as well as the amplitude, and we consider the pulse evolution in a reference frame moving with the group velocity of the fundamental mode, so that in the absence of dispersion a pulse would stay centred at time

$t = 0$ throughout its propagation. Finally, we use units such that $|\mathbf{E}(\mathbf{x}, t)|^2$ is the field intensity in W/m$^2$. The envelope function can then be expanded into a superposition of individual modes $p = 0, 1, 2, ...$, each represented by a discrete transverse fibre mode profile $\mathbf{F}_p(x, y)$ and a modal envelope $A_p(z, t)$, as

$$\mathbf{E}(\mathbf{x}, t) = \sum_p \frac{\mathbf{F}_p(x, y)}{\left[\int \mathrm{d}x\, \mathrm{d}y\, |\mathbf{F}_p|^2\right]^{1/2}} A_p(z, t). \tag{1}$$

Note that $|A_p(z, t)|^2$ gives the instantaneous power propagating in mode $p$ in units of W, and that a simplified normalisation has been used compared to a more rigorous previous formulation (Poletti & Horak, 2008). The accuracy of this approximation improves as the fibre core size is increased and the core-cladding index contrast is decreased, leading to guided modes with an increasingly negligible longitudinal component of polarisation.
The multimode generalised nonlinear Schrödinger equation (MM-NLSE) is then given by the following set of coupled equations to describe the dynamics of the mode envelopes,

$$\begin{aligned}\frac{\partial A_p}{\partial z} &= \mathcal{D}\{A_p\} \\ &+ i\frac{n_2\omega_0}{c}\left(1 + \frac{i}{\omega_0}\frac{\partial}{\partial t}\right)\sum_{l,m,n}\left\{(1 - f_R)S^K_{plmn}A_l A_m A^*_n + f_R S^R_{plmn}A_l[h * (A_m A^*_n)]\right\}.\end{aligned} \tag{2}$$

The following approximations have been applied here: (i) we have assumed that the Raman response and the pulse envelope functions vary slowly on the time scale of a single cycle of the carrier wave, so that we can neglect a rapidly oscillating term, and (ii) an additional term related to the frequency dependence of the mode functions has been omitted, assuming the variation of $S^{K,R}_{plmn}$ is slow compared to the $1/\omega_0$ self-steepening term. In Eq. (2),

$$\mathcal{D}\{A_p\} = i(\beta_0^{(p)} - \Re[\beta_0^{(0)}])A_p - (\beta_1^{(p)} - \Re[\beta_1^{(0)}])\frac{\partial A_p}{\partial t} + i\sum_{n\geq 2}\frac{\beta_n^{(p)}}{n!}\left(i\frac{\partial}{\partial t}\right)^n A_p \tag{3}$$

yields the effects of dispersion of mode $p$ with coefficients $\beta_n^{(p)} = \partial^n\beta^{(p)}/\partial\omega^n$. Here we allow for complex values of the modal propagation constants $\beta^{(p)}$ where the imaginary part describes mode and wavelength dependent losses; $\Re[..]$ denotes the real part only. The second line of (2) represents the effects of optical nonlinearity with a nonlinear refractive index $n_2$. The term $\propto \partial/\partial t$ describes self-steepening and the two terms within the sum describe Kerr and Raman nonlinearities. The Raman term contributes with a fraction $f_R$ to the overall nonlinearity ($f_R = 0.18$ for silica glass fibres) and contains the Raman mode overlap factors

$$S^R_{plmn} = \frac{\int \mathrm{d}x\, \mathrm{d}y\, \left[\mathbf{F}^*_p \cdot \mathbf{F}_l\right]\left[\mathbf{F}_m \cdot \mathbf{F}^*_n\right]}{\left[\int \mathrm{d}x\, \mathrm{d}y\, |\mathbf{F}_p|^2 \int \mathrm{d}x\, \mathrm{d}y\, |\mathbf{F}_l|^2 \int \mathrm{d}x\, \mathrm{d}y\, |\mathbf{F}_m|^2 \int \mathrm{d}x\, \mathrm{d}y\, |\mathbf{F}_n|^2\right]^{1/2}} \tag{4}$$

as well as a convolution of the time dependent Raman response function $h(t)$ with two mode amplitudes

$$[h * (A_m A^*_n)](z, t) = \int \mathrm{d}\tau\, h(\tau)A_m(z, t - \tau)A^*_n(z, t - \tau). \tag{5}$$

The mode overlap factors responsible for the instantaneous Kerr effect are given by

$$S^K_{plmn} = \frac{2}{3} S^R_{plmn} + \frac{1}{3} \frac{\int \mathrm{d}x\,\mathrm{d}y \left[\mathbf{F}^*_p \cdot \mathbf{F}^*_n\right]\left[\mathbf{F}_m \cdot \mathbf{F}_l\right]}{\left[\int \mathrm{d}x\,\mathrm{d}y\,|\mathbf{F}_p|^2 \int \mathrm{d}x\,\mathrm{d}y\,|\mathbf{F}_l|^2 \int \mathrm{d}x\,\mathrm{d}y\,|\mathbf{F}_m|^2 \int \mathrm{d}x\,\mathrm{d}y\,|\mathbf{F}_n|^2\right]^{1/2}}. \tag{6}$$

Numerically, the mode functions of all the modes involved in the nonlinear effects under consideration are first evaluated at $\omega_0$ and a table of overlap integrals is calculated. The number of modes and overlap integrals can be greatly reduced based on mode symmetry arguments (Poletti & Horak, 2008); all the applications discussed in the following will employ such reduced sets of modes. Next, the dispersion curves for these modes are calculated. Finally, the system of equations (2) is integrated numerically using a standard symmetrised split-step Fourier method (Agrawal, 2001), where adaptive step size control is implemented by propagating the nonlinear operator using a Runge-Kutta-Fehlberg method (Press et al., 2006). In order to avoid numerical artifacts, we also found it necessary to further limit the maximum step size to a fraction of the shortest beat length between all the modes considered. The accuracy and convergence of the results is further checked by running multiple simulations with increasingly small longitudinal step sizes.

The framework presented above still allows for modes of arbitrary polarisation. In most practical situations, however, one is interested in a subset of modes representing only a specific polarisation state which is determined by the pump laser. The two most common cases are briefly discussed in the following.

### 2.1 Circular polarisation

Under the weak guiding condition, modes fall into groups of $LP_{mn}$ modes containing either two ($m = 0$) or four ($m > 0$) degenerate modes. Within each group, the modes can be combined into modes that are either $\sigma_+$ or $\sigma_-$ circularly polarised at every point in the fibre. If the light launched into the fibre is, for example, $\sigma_+$ polarised, the form of the overlap integrals (4) and (6) guarantees that no light is coupled into the $\sigma_-$ polarised modes during propagation and those modes can therefore be eliminated entirely from the model. It is worth emphasising that this is an *exact result* within the weak guiding limit. Using the properties of circular polarisation vectors, the overlap integrals are then simplified to

$$\begin{aligned} S^R_{plmn} &= \frac{\int \mathrm{d}x\,\mathrm{d}y\, F_p F_l F_m F_n}{\left[\int \mathrm{d}x\,\mathrm{d}y\, F_p^2 \int \mathrm{d}x\,\mathrm{d}y\, F_l^2 \int \mathrm{d}x\,\mathrm{d}y\, F_m^2 \int \mathrm{d}x\,\mathrm{d}y\, F_n^2\right]^{1/2}}, \\ S^K_{plmn} &= \frac{2}{3} S^R_{plmn}, \end{aligned} \tag{7}$$

where the mode functions have been written as $\mathbf{F}_p = \mathbf{e}_+ F_p$ for $\sigma_+$ polarised modes with real-valued scalar mode functions $F_p$.

### 2.2 Linear polarisation

The situation is slightly more complicated in the case of linearly polarised pump light. In this case, nonlinear coupling between orthogonal polarisation modes is in principle allowed, leading to, for example, birefringent phase matching and vector modulation instability (Agrawal, 2001; Dupriez et al., 2007). However, for many practical situations where modes can be described as $LP_{mn}$ modes, if linearly polarised light is launched into the fibre, nonlinear coupling to orthogonal polarisation states is effectively so small that most of the pulse energy remains in its original polarisation throughout the entire pulse propagation. This allows

halving the number of modes to be considered in the model with significant computational advantage, and a simpler definition of the overlap factors (4) and (6). There are several important practical situations where this approximation can be acceptable:
(i) For degenerate modes (no birefringence), the overlap factor (6) for four-wave mixing (FWM) between modes of parallel polarisation is three times larger than that for orthogonal polarisation. Since the dispersion properties, and therefore the phase matching conditions, are the same, nonlinear gain is much higher for the same polarisation and thus will dominate the dynamics.
(ii) For few-moded fibres power transfer to orthogonal modes by FWM can be negligible if either the phase matching condition cannot be fulfilled at all, or if the phase matching condition is achieved only for widely separated wavelength bands where the difference in group velocities limits the effective interaction length due to walk-off effects.
In these situations one can therefore use an approximate theoretical description of pulse propagation by restricting the MM-NLSE to the $LP_{mn}$ modes of the fibre with the same linear polarisation everywhere. Assuming real-valued $x$-polarised mode functions $\mathbf{F}_p = \mathbf{e}_x F_p$, the overlap integrals then reduce to

$$S^R_{plmn} = S^K_{plmn} = \frac{\int \mathrm{d}x\,\mathrm{d}y\, F_p F_l F_m F_n}{\left[\int \mathrm{d}x\,\mathrm{d}y\, F_p^2 \int \mathrm{d}x\,\mathrm{d}y\, F_l^2 \int \mathrm{d}x\,\mathrm{d}y\, F_m^2 \int \mathrm{d}x\,\mathrm{d}y\, F_n^2\right]^{1/2}}. \tag{8}$$

A further simplification is also sometimes possible. If linearly polarised light is predominantly launched in an $LP_{0n}$ mode, power transfer into $LP_{mn}$ modes with $m > 0$ can only be initiated by spontaneous FWM processes. By contrast, other $LP_{0n}$ modes of the same polarisation can be excited by stimulated processes, see Sec. 3.1. Thus, if the dominant processes within the pulse propagation are stimulated ones, e.g., in the regime of high powers and relatively short propagation distances, the study can be effectively restricted to $LP_{0n}$ modes with the same polarisation.

## 3. Supercontinuum generation in multimode fibres

One of the first applications where the MM-NLSE presented in the previous section can provide deep insights is that of supercontinuum (SC) generation in multimode fibres. As already mentioned, the complex dynamic underlying SC generation in *singlemode* fibres is by now well understood. Octave spanning SC in suitably designed fibres arises as a combination of various nonlinear phenomena, including soliton compression and fission, modulation instability, parametric processes, intrapulse Raman scattering, self phase modulation (SPM) and cross phase modulation (XPM) (Dudley et al., 2006). As the fibre diameter is increased though, as required for example to increase the SC power spectral density without destroying the fibre, the fibre starts to support multiple modes. Previous theoretical models were usually restricted to two polarisation modes of a birefringent fibre (Agrawal, 2001; Coen et al., 2002; Lehtonen et al., 2003; Martins et al., 2007) or included a maximum of two spatially distinct modes (Dudley et al., 2002; Lesvigne et al., 2007; Tonello et al., 2006). Using the full MM-NLSE, however, fibres with arbitrary modal contents can be studied, for which a rich new list of *intermodal* nonlinear phenomena emerges, causing the transfer of nonlinear phase and/or power between selected combinations of modes (Poletti & Horak, 2009).
In this section, using simulations of a specific few-moded fibre as an illustrative example, we will discuss how modal symmetries and launch conditions can have a drastic influence on intermodal power transfer dynamics. For pump peak powers in the range of tens to hundreds

of kW, if the nonlinear length of the pump pulses is shorter than the walk-off length between the modes involved, significant power transfer into high-order modes with the appropriate symmetry can occur, which can be beneficial, for example, to further extend the SC spectrum to shorter wavelengths. Even if conditions for significant intermodal power transfer are not met, it is found that intermodal XPM can still play a significant role in the SC dynamics by broadening the spectrum of modes which would not otherwise present a significant spectral broadening if pumped on their own.

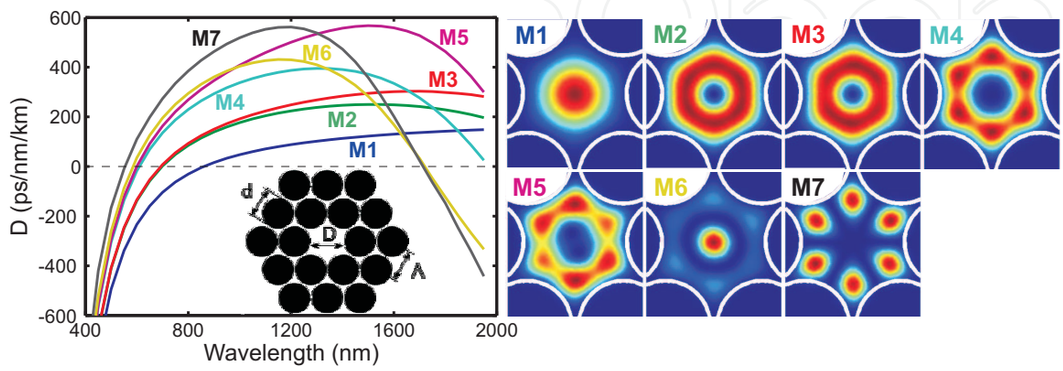


Fig. 1. GVD curves and transverse mode functions, calculated at 850nm, of the 7 circularly polarised modes guided in a HF with $\Lambda = 2.7\mu$m and $d = 2.5\mu$m .

To discuss the intermodal nonlinear dynamics leading to SC generation we focus on a *moderately* multimoded holey fibre (HF) consisting of two rings of large circular air holes with pitch $\Lambda = 2.7\mu$m and relative hole size $d/\Lambda = 0.93$, surrounding a solid core with a diameter of a few optical wavelengths ($D = 2\Lambda - d = 2.9\mu$m ), see Fig. 1. From 400nm to 2000nm the fibre supports 14 modes with effective areas ranging between 3.6 and $6.1\mu\text{m}^2$. To reduce the computational time it is possible to combine these modes into 7 pairs of circularly polarised modes and to exploit the forbidden power exchange between modes with opposite circular polarisation (see Sec. 2.1), only to focus on the 7 right-handed circularly polarised modes M1, M2,..., M7 shown in Fig. 1. The group velocity dispersion (GVD) curves of these modes are significantly different from each other, with a first zero dispersion wavelength (ZDW) ranging from $\lambda_7 = 550$nm for M7 to $\lambda_1 = 860$nm for M1.

### 3.1 Effect of modal symmetries and launch conditions on intermodal power transfer

Equation (2) shows that the transfer of power between modes is mediated by FWM terms of the form $S^K_{plmn} A_l A_m A^*_n$, with $l, m \neq n$. If only a single mode $l$ is initially excited with a narrow spectral line, the strongest power transfer to mode $p$ and therefore the first to be observed in the nonlinear process is the one controlled by *degenerate* FWM terms of the form $S^K_{plln} A_l A_l A^*_n$. If both modes $p$ and $n$ are initially empty, power transfer starts with a spontaneous FWM process and is therefore slow. If one of the generated photons is however returned into the pump $l$ by *stimulated emission*, the process becomes much faster and tends to dominate the nonlinear dynamics in the limit of high-power pulse propagation over short distances. Interestingly, these $S^K_{plll} A_l A_l A^*_l$ processes produce automatic phase-locking of mode $p$ to the pump mode $l$, similarly to what happens in non-phase matched second and third harmonic generation processes (Roppo et al., 2007). However, processes $S^K_{plll}$ require (i) that modes $p$ and $l$ belong to the same symmetry class, and (ii) that they present a large overlap. For the HF

under investigation these conditions are only fulfilled for the two $LP_{0n}$ modes M1 and M6, and therefore one would expect significant power transfer only between them.

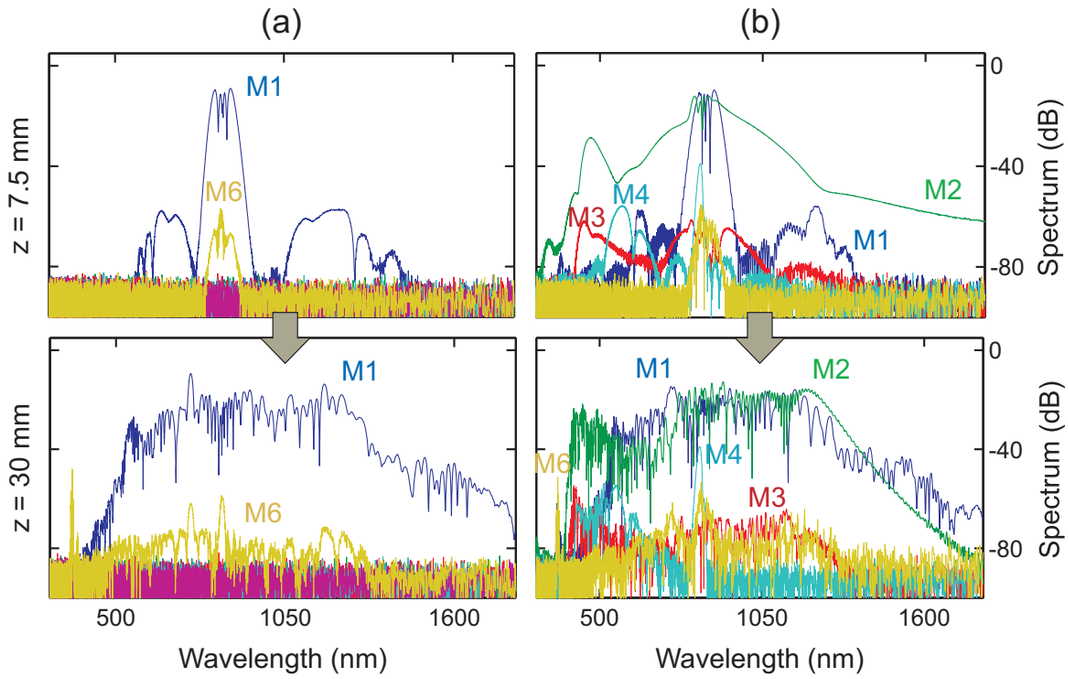


Fig. 2. Simulations of multimode nonlinear propagation in the HF of Fig. 1 after 7.5mm (top row) and 30mm (bottom row), for a 100fs sech-shaped pump centred at 850nm. (a) Only M1 is excited and (b) both M1 and M2 are excited with a 50kW peak power pulse.

This expected behaviour is indeed confirmed by the numerical simulation shown in Fig. 2(a), where a hyperbolic secant pump pulse with temporal profile $A_p(0,t) = \sqrt{P_0}\,\mathrm{sech}(\mathrm{t}/\mathrm{T}_0)$ with $T_0 = 100$fs (full width at half maximum 176fs) and centred at $\lambda_p = 850$nm is launched into M1 only and propagated through 30mm of the HF. Here the pulse peak power $P_0$ is set to 50kW, corresponding to a 10nJ pulse and, for mode M1, to a soliton of order $N = 166$. As one would expect from single mode SC theory (Dudley et al., 2006), besides SPM-induced spectral broadening, such a high-$N$ pulse develops sidebands which grow spontaneously from noise, through an initial modulation instability (MI) process. The characteristic distance of this phenomenon $L_{MI} \sim 16L_{NL} = 16\lambda/(3\pi n_2 S^K_{1111} P_0) = 6.9$mm correlates well with the simulation results. As expected, of all the other 6 modes only M6 is significantly amplified at wavelengths around $\lambda_p$, and subsequently develops a wide spectral expansion and an isolated peak at 360nm. Further analysis of spectrograms and phase matching conditions indicates that this peak is a dispersive wave in M6, phase matched to a soliton in M1 and slowly shifting to shorter wavelengths as the soliton red-shifts due to the effect of intrapulse Raman nonlinearity. Under these launching conditions the study can thus be restricted to the $LP_{0n}$ modes of the fibre without loss of accuracy. Simulations also show that if either M2, M3, M4, M5 or M7 are selectively launched, no power is transferred to any of the other modes, and each of them evolves as in the single mode case.

When two or more modes contain a significant amount of power, they can all act as pumps for weaker modes. Moreover, if these modes belong to different symmetry classes, additional

FWM terms come into play, giving rise to a much richer phenomenology. As an example, Fig. 2(b) shows what happens when both M1 and M2 are simultaneously excited with a $P_0 = 50$kW sech pulse. This pulse corresponds to an $N = 27$ soliton for M2, due to its much larger value of $\beta_2^{(2)}$ at the pump wavelength. As a result, the SC generated in M2 has a more temporally coherent nature, as it originates from soliton compression and fission mechanisms (the fission length $L_{\text{fiss}} = N \cdot L_{\text{NL}}$ is around 16mm). Due to a shorter ZDW than M1, the final SC in M2 also extends to much shorter wavelengths than the one in M1 (400nm versus 550nm, respectively), which can be one of the benefits of using multimode fibres for SC generation. Moreover, in addition to M6, also M3 and M4 are amplified from noise, generating a complex output spectrum, where the final relative magnitude of different modes is a strong function of wavelength. This is reminiscent of early experimental results (Delmonte et al., 2006; Price et al., 2003).

### 3.2 Non-phase matched permanent intermodal power transfer

To understand the complex dynamics of intermodal power transfer it is useful to refer to the approximate analytical theory of cw pumped parametric processes, which neglects the effects of GVD and pulse walk-off but still provides a valid reference (Stolen & Bjorkholm, 1982). Within this framework, parametric gain leading to exponential signal amplification requires the propagation constant mismatch $\Delta\beta_{plmn} = \beta^{(l)}(\omega_l) + \beta^{(m)}(\omega_m) - \beta^{(p)}(\omega_p) - \beta^{(n)}(\omega_n)$ to be smaller than a few times the *average* inverse nonlinear length $1/L_{NL} = \overline{\gamma}P_0$.

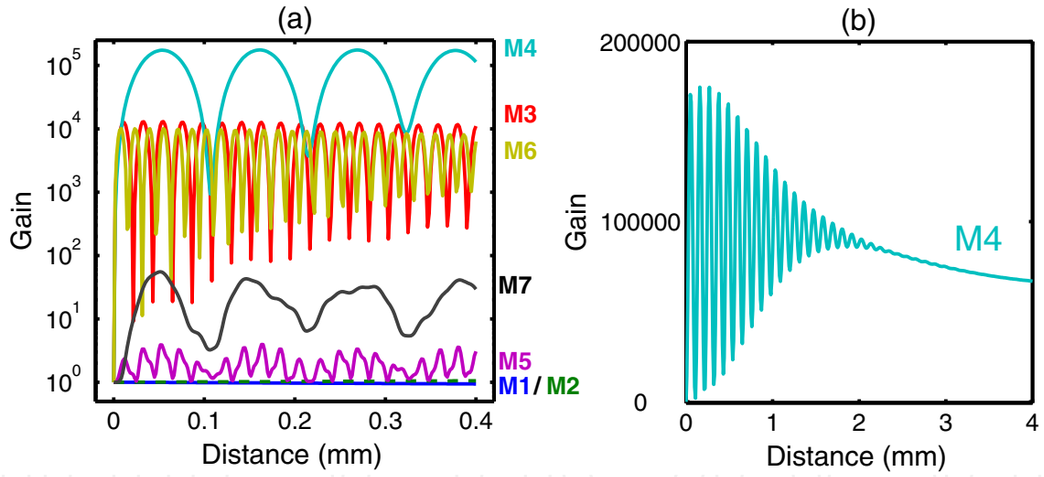


Fig. 3. (a) Dynamic gain evolution for each individual mode when M1 and M2 are simultaneously excited at launch as in Fig. 2(b), showing the oscillatory behaviour typical of non-phase matched parametric processes. (b) Permanent power transfer to M4 despite the lack of parametric phase matching due to walk-off between the pumps in M1 and M2 and the signal in M4.

For multimode processes, an estimate of $\overline{\gamma}$ can be obtained by averaging all the intermodal nonlinearities $\gamma_{plmn} = \frac{3\pi n_2}{\lambda} S^K_{plmn}$ which contribute to SPM and XPM between the relevant modes. However, in most practical situations involving SC generation in highly nonlinear multimode fibres, $\Delta\beta_{plmn} \gg \overline{\gamma}P_0$ for all the relevant FWM processes considered. Thus, no parametric gain is typically observed and each FWM term leads to an oscillatory power exchange between modes, as shown by the dynamic gain curves of high order modes when

only M1 and M2 are initially pumped, reported in Fig. 3(a). The oscillation periods are given by the beat lengths $L_b \sim 2\pi/|\Delta\beta|$. For example, for the process leading to amplification of M6, $\Delta\beta_{6111} = 4.1 \cdot 10^5$ m$^{-1}$, corresponding to a value of $L_b = 15.3\mu$m in agreement with the simulation. For modes amplified by a cascade of intermodal FWM processes, such as M5 and M7 in the example, the signature of multiple beating frequencies can be clearly observed.
Despite the non-phase matched nature of most FWM processes, simulations show that after long enough propagation some power is *permanently* transferred into the weaker modes. This is shown, for example, in Fig. 3(b) extending the propagation distance of M4 from 0.4mm to 4mm. A more detailed analysis excluding XPM and Raman effects found this behaviour to be uniquely caused by the temporal walk-off between the pulses involved. The typical length scale of this permanent power transfer is therefore of the order of the walk-off length of all the pulses involved, given by $L_W^{pq} = T_0/|1/v_g^{(p)} - 1/v_g^{(q)}| = T_0/|\beta_1^{(p)} - \beta_1^{(q)}|$ for modes $p$ and $q$. For the example in Fig. 3(b), $L_W^{12} = 3$mm, $L_W^{24} = 2.4$mm and $L_W^{14} = 1.3$mm, which correlate well with the simulation.
In conclusion, nonlinear intermodal power transfer is governed by two length scales, a beat length leading to fast initial power oscillations and a walk-off length leading to permanent power transfer. In order to observe in practice intermodal nonlinear effects, the nonlinear length of the pump pulses must be shorter than the walk-off length, i.e., high peak powers are required. Otherwise, nominally multimode fibres can exhibit the same nonlinear behaviour as singlemode ones. Scaling a fixed fibre structure to larger core sizes allows for larger power throughput, but at the same time longer beat and walk-off lengths lead to much stronger mode coupling, and significant amounts of power can be transferred into higher order modes. In this case, as shown in Fig. 2, higher order modes may also serve to extend the SC spectral extension to much shorter wavelengths.

### 3.3 Effect of intermodal cross phase modulation

Intermodal power transfer mediated by FWM terms, which can permanently exchange power between modes even in the absence of proper phase matching, is not the only intermodal nonlinear effect which can occur in a multimode fibre. Intermodal XPM can also play a role in significantly broadening the spectrum of a mode which would not undergo a significant spectral expansion if propagated on its own (Chaipiboonwong et al., 2007; Schreiber et al., 2005).
To illustrate this phenomenon, we simulate the propagation of a pulse launched in M1 and/or M2 at 725nm, where M1 is in the normal dispersion region and M2 is in the anomalous region. In order to observe significant spectral expansion and intermodal effects within the distance where the pulses are temporally overlapped, we increase the input power up to a value of $P_0 = 500$kW, close to the estimated fibre damage threshold.
Figs. 4(a) and (b) show that when M1 is individually launched, only some SPM-based spectral expansion is visible, whereas if only M2 is launched, a wide MI-based SC develops. On the other hand, if the same input pulse is launched simultaneously in *both* modes as in Fig. 4(c), a much wider output spectrum is developed also in M1. Under these operating conditions the intermodal power transfer is negligible, as confirmed by nearly identical spectral results obtained when all $S_{plmn}^K$ and $S_{plmn}^R$ coefficients responsible for intermodal FWM are set to zero. Therefore, the increased spectral expansion in M1 must be generated by intermodal XPM effects alone. This is indeed confirmed by the simulation in Fig. 4(d), showing that when all intermodal XPM effects are artificially switched off, M1 and M2 produce a very similar spectrum to that of their individual propagation.

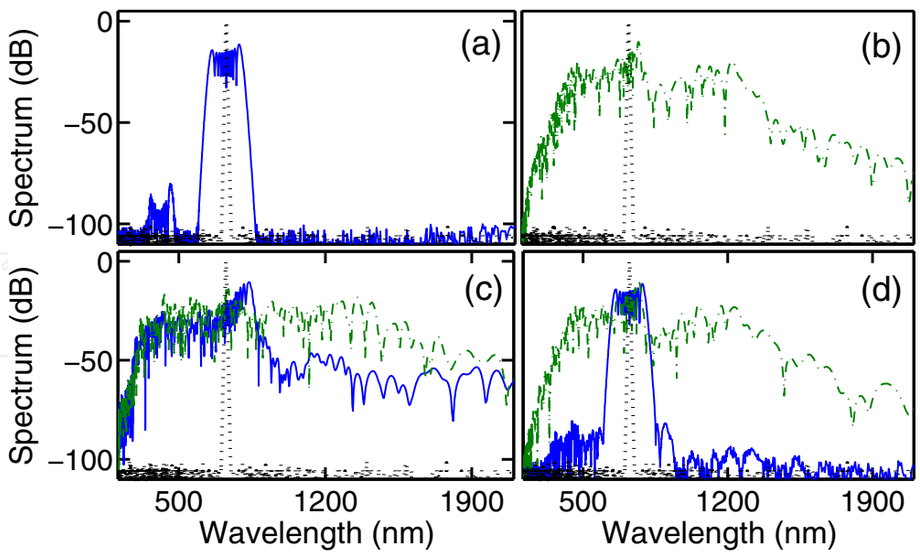


Fig. 4. Spectral output after 2mm propagation in the HF of Fig. 1 of a $T_0 = 100$fs and $P_0 = 500$kW sech pulse centred at 725nm and launched in: (a) M1 only (blue, solid line); (b) M2 only (green, dashed-dot line); (c) both M1 and M2, and (d) both M1 and M2 when all intermodal XPM coefficients are artificially set to zero. The input pulse is shown as a black dotted line.

## 4. Self-focusing in optical fibres in a modal picture

For laser powers larger than discussed in the previous section and into the MW regime, the nonlinear refractive index induced in the glass by the laser may become strong enough to introduce significant spatial reshaping of the beam in the transverse direction. The refractive index of a material is given by $n_0 + n_2 I$, including both the linear, $n_0$, and nonlinear term, $n_2$, and where $I$ is the position-dependent intensity of the laser. Thus, if the beam has a Gaussian-like transverse profile and the optical Kerr nonlinearity $n_2$ is positive, as is the case in most of the commonly used transparent materials, the induced nonlinear refractive index is maximum at the centre of the beam and decreases towards the pulse edges. Therefore, the induced index profile forms a focusing lens, acting back on the laser beam itself. This effect is known as *self-focusing* and has been studied extensively in bulk materials for nearly 50 years (Askaryan, 1962; Chiao et al., 1964). For input powers $P$ below a critical power $P_{crit}$, self-focusing is finally overcome by the beam divergence. In the case of $P > P_{crit}$, however, the pulse undergoes catastrophic collapse leading to permanent damage of the material (Gaeta, 2000). The critical power is given by

$$P_{crit} = 1.86 \frac{\lambda^2}{4\pi n_0 n_2}, \tag{9}$$

where the numerical factor slightly depends on the beam profile in a bulk material (Fibich & Gaeta, 2000). Numerically, self-focusing in bulk media is most commonly modelled by slowly-varying envelope models or, more accurately, by a nonlinear envelope equation (NEE) describing the dynamics of the transverse beam profile $\Phi(\mathbf{x}, t)$ (Brabec & Krausz, 1997;

Ranka & Gaeta, 1999),

$$\frac{\partial}{\partial z}\Phi = \mathcal{D}_{mat}\{\Phi\} + \frac{i}{2\beta_0}\left(1+\frac{i}{\omega_0}\frac{\partial}{\partial t}\right)^{-1}\nabla_\perp^2\Phi + i\frac{n_2 n_0\omega_0}{2\pi}\left(1+\frac{i}{\omega_0}\frac{\partial}{\partial t}\right)|\Phi|^2\Phi, \quad (10)$$

where $\mathcal{D}_{mat}\{\Phi\}$ is a dispersion term similar to (3) describing the effect of material dispersion and $\nabla_\perp^2$ is the transverse Laplace operator. The NEE incorporates many features similar to the MM-NLSE (2), e.g., higher order dispersion, Kerr nonlinearity and self-steepening terms. However, even in the presence of rotational symmetry, the envelope function $\Phi$ is a two-dimensional object (radial and temporal coordinate), in contrast to the MM-NLSE which only uses a finite number of one-dimensional (temporal) envelope functions to describe the same situation. If the number of modes is small, the MM-NLSE is thus computationally significantly more efficient, both in terms of reduced memory requirements and faster dynamics simulation.

It is now well established that the same process of self-focusing occurs in optical waveguides and fibres and that the same power threshold for catastrophic collapse applies (Farrow et al., 2006; Gaeta, 2000). However, for powers below $P_{crit}$ the observed light propagation behaviour is qualitatively different from that observed in bulk media, since here the light is additionally bound by total internal reflection at the core-cladding interface, which can lead to additional spatial and temporal interference and dispersion effects, such as periodic oscillations of the beam profile or catastrophic pulse collapse even when the launched peak power is below the critical value. In this section we will discuss these effects within the framework of the MM-NLSE, which leads to an easy understanding of fibre-based self-focusing within a modal picture (Horak & Poletti, 2009; Milosevic et al., 2000). Such an interpretation is particularly useful in the context of high-power fibre lasers, which now achieve peak powers close to the critical power with pulse lengths approaching the nanosecond regime (Galvanauskas et al., 2007).

### 4.1 Continuous wave limit

We start our discussion with the case of cw propagation, which in practice is also a good approximation to the behaviour of long pulses (ps to ns regime) near the pulse peak, and use the MM-NLSE restricted to the linearly polarised $LP_{0n}$ modes, as discussed in Sec. 2.2. The MM-NLSE thus reduces to

$$\frac{\partial A_p}{\partial z} = i(\beta_0^{(p)} - \beta_0^{(0)})A_p + i\frac{n_2\omega_0}{c}\sum_{l,m,n} S^K_{plmn}A_l A_m A_n^* \quad (11)$$

with $S^K_{plmn}$ given by (8). Specifically, we assume propagation in a short piece of a step-index fibre with a pure silica core of 40$\mu$m diameter and a refractive index step of 0.02 between core and cladding. This fibre is similar to photonic crystal large-mode area fibres which are commercially available, where the index step has been increased such that the fibre supports eight $LP_{0n}$ modes. The zero-dispersion wavelength of this fibre is at 1.26$\mu$m, and we assume a pump laser operating at 1300nm wavelength. The critical power (9) for silica at this wavelength is $P_{crit} = 5.9$MW. Note that at this power level pulses up to approximately 100ps length can be transmitted through the fibre without fibre damage (Stuart et al., 1996).

Figure 5 shows the dynamics of light propagation along this fibre when cw light is launched into the fundamental $LP_{01}$ mode with a power of $0.7P_{crit}$=4.84MW. The curves in Fig. 5(a) show the power $|A_p|^2$ in the lowest order modes obtained by solving Eq. (11). Power

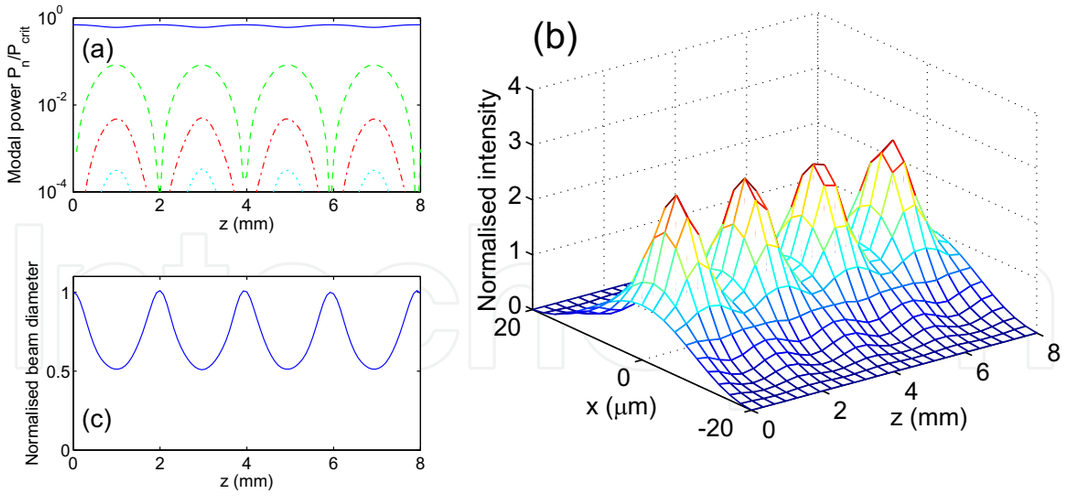


Fig. 5. Propagation of cw laser light at 1.3$\mu$m wavelength through a multimode silica step-index fibre with 40$\mu$m core diameter and core-cladding index difference of 0.02. The launched power is $0.7P_{crit}$=4.84MW in the fundamental $LP_{01}$ mode. (a) Power in the lowest four fibre modes versus propagation distance. (b) 2D (transverse and longitudinal) spatial intensity profile of the beam. (c) Dynamics of the transverse beam width (FWHM), normalised to the width of the fundamental fibre mode.

from the fundamental mode is quickly transferred over sub-mm propagation distances into higher order modes by FWM processes, most prominently by induced FWM involving three pump photons as described by terms of the form $\partial A_p/\partial z \propto iA_0^2A_0^*$, see Sec. 3.1. However, because of the phase mismatch $\beta_0^{(p)} - \beta_0^{(0)}$ between the fundamental mode and the higher order modes the initial FWM gain is reversed after a certain propagation distance (about 1mm for the chosen parameters) and power is coherently transferred back into the pump from the higher order modes. This process is repeated subsequently leading to a periodic exchange of power between modes. The phase mismatch increases for increasing mode order and thus the maximum transferred power decreases.

In Fig. 5(b) we depict the corresponding 2D beam intensity $|\mathbf{E}(x,z)|^2$ calculated by summing the modal contributions (1), normalised to the maximum field $|\mathbf{E}(0,0)|^2$ at the fibre input. The field experiences significant periodic enhancement on the beam axis at positions where large fractions of the total power propagate inside higher order $LP_{0n}$ modes. At these positions of enhanced intensity, the full width at half maximum (FWHM) of the beam profile is strongly reduced, as shown in Fig. 5(c). The intermodal FWM processes together with the modal phase mismatch are therefore responsible for periodic beam self-focusing and defocusing in a fibre. This complements the standard interpretation of self-focusing in a bulk medium using Gaussian beam propagation, which describes the same phenomenon as focusing by a Kerr-induced lensing effect, followed by beam divergence and subsequent total internal reflection at the core-cladding interface. We finally note that a stationary solution can be obtained for the cw MM-NLSE in which the modal amplitudes and phases are locked in such a way that no oscillations occur. In the bulk interpretation this corresponds to the situation where nonlinear focusing and diffraction are perfectly balanced, thereby generating a stationary spatial soliton.

It may seem that this modal description of self-focusing is only possible in multimode fibres but breaks down in singlemode fibres, for example in large-mode area photonic crystal fibres

designed for endlessly single mode operation (Mortensen et al., 2003). However, in this case the role of the higher order bound modes of a multimode fibre is taken over by the cladding modes, and it is the FWM-induced power exchange between the guided mode of a singlemode fibre and its cladding modes which provides a modal interpretation of self-focusing.

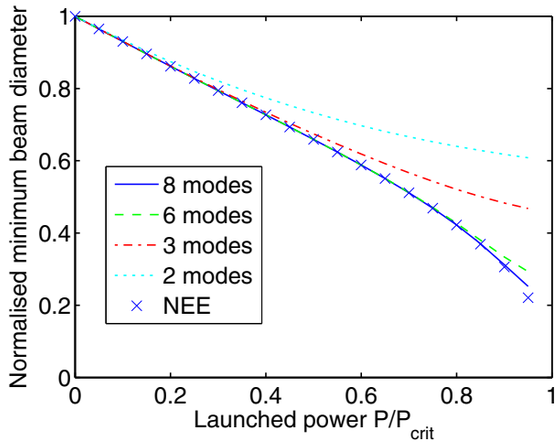


Fig. 6. Minimum beam diameter during the first period of self-focusing oscillation under cw pumping vs pump power for the same fibre parameters as in Fig. 5. The curves correspond to MM-NLSE simulations involving the lowest 2, 3, 6 modes only, and all 8 $LP_{0n}$ modes (from top to bottom). The crosses indicate simulation results using the nonlinear envelope equation.

Using only a finite number of modes in the simulation of the MM-NLSE necessarily limits the transverse spatial resolution that can be achieved by this method. For example, the $LP_{0n}$ mode function exhibits $n$ maxima and $n-1$ zeros along the radial direction within the fibre core region. With simulations using $n$ different modes one can therefore expect a maximum resolution of the order of $R/n$ where $R$ is the core radius. Simulations with pump powers approaching the critical power $P_{crit}$ will thus require a larger number of modes in order to correctly describe the increasingly small minimum beam diameter. We investigate this behaviour in Fig. 6. Here we show the minimum beam diameter achieved during the first period of self-focusing and diffraction, i.e., at approximately 1mm of propagation for the parameters of Fig. 5, when the MM-NLSE is restricted to different numbers of modes. For clarity, the beam diameter is normalised to the diameter of the launched beam ($LP_{01}$ mode). We observe that simulations with 2, 3, and 6 modes are accurate up to pump powers of approximately $0.2P_{crit}$, $0.4P_{crit}$, and $0.8P_{crit}$, respectively, compared to simulations involving all 8 bound fibre modes of this sample fibre. For comparison, we also show the results of the NEE beam propagation method (10). This confirms the accuracy of the MM-NLSE with 8 modes up to $0.95P_{crit}$ corresponding to a nearly five-fold spatial compression of the beam.
For the simulations shown in Fig. 6 we used the same 4th-5th order Runge-Kutta integration method with adaptive step size control (MATLAB R2010b by MathWorks, Inc.) for both the MM-NLSE and the NEE. Each data point required approximately 0.9s of CPU time on a standard desktop computer with the 8-mode MM-NLSE and $<$0.2s with 6 modes. In contrast, the corresponding NEE simulations with 1024 radial grid points required 101s, that is, two to three orders of magnitude slower than the MM-NLSE.

### 4.2 Short pulse propagation

Next, we consider the propagation of short pulses in the regime of peak powers close to the critical power, where in addition to transverse spatial effects the pulse may exhibit complex temporal dynamics related to intermodal and intramodal dispersion, self-steepening and nonlinear effects. As an example we consider sech-shaped pulses with a temporal FWHM of 100fs launched with a peak power of $0.8P_{crit}$ into the fundamental mode of the multimode fibre considered above. The pump wavelength is again set to $1.3\mu$m. The simulations discussed in the following used a 6-mode MM-NLSE with 2048 temporal grid points solved with a split-step Fourier method (Poletti & Horak, 2008; 2009).

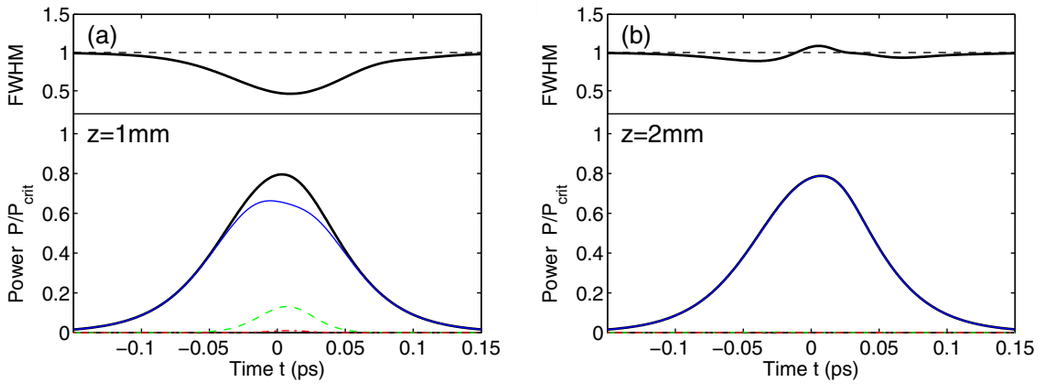


Fig. 7. Propagation of a 100fs sech-shaped pulse with $0.8P_{crit}$ peak power at $1.3\mu$m wavelength with the same fibre parameters as in Fig. 5 after (a) 1mm and (b) 2mm of propagation. The bottom part of the figure shows the overall temporal pulse profile (thick solid line) as well as its contributions from the fundamental mode (thin solid), first (dashed) and second (dash-dotted) higher order modes. The top part of the figure shows the spatial FWHM beam diameter along the pulse, normalised to the FWHM of the fundamental mode.

The initial dynamics of the pulse propagation are shown in Fig. 7. After 1mm of propagation, Fig. 7(a), a significant amount of power has been transferred from the fundamental mode into the higher order modes, leading to a transverse beam focusing to approximately 40% of the input beam width. The transverse beam size depends on the pulse power and thus varies along the pulse shape: the beam diameter is smallest near the temporal peak of the pulse, but remains unchanged in the trailing and leading edges where the power is low. Propagating further to 2mm, Fig. 7(b), most of the power has been converted back into the fundamental mode, similar to the cw case of Fig. 5. However, the transfer is not complete and is not uniform along the pulse. This is related to the walk-off of the higher order modes because of intermodal dispersion as well as a slight dependence of the beam oscillation period on power. Therefore, the spatial FWHM of the beam at 2mm propagation length is below that of the fundamental mode in some parts of the pulse while it exceeds it in other parts.

Continuing the propagation of Fig. 7, the spatial beam variations persist, but the deviations from a simple oscillation become more prominent. This is shown clearly in Fig. 8(a) in the beam properties after 7mm of propagation. At this point the initial sech-shaped temporal profile has steepened on the trailing edge and an ultrashort pulse peak is forming due to the interference of the modal contributions. In particular, the first high order mode exhibits a similar power level as the fundamental mode. Simultaneously, the beam diameter is strongly reduced. At 7.4mm of propagation, Fig. 8(b), this peak has narrowed further and reaches

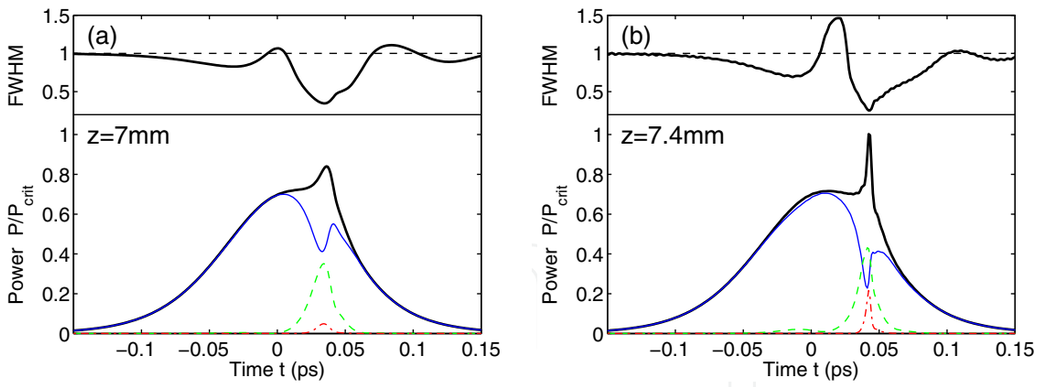


Fig. 8. Continuation of the pulse propagation of Fig. 7 to (a) 7mm and (b) 7.4mm of fibre length exhibiting simultaneous spatial and temporal collapse.

the critical power for catastrophic collapse while the beam diameter has reduced to 20% of the fundamental mode. For even longer propagation lengths the simulations show the pulse breaking up into many ultrashort high-intensity parts around this initial instability, however the MM-NLSE with 6 modes becomes invalid at this point due to its limited spatial and temporal resolution. Simulations with the MM-NLSE restricted to the fundamental mode reveal only a very small amount of pulse reshaping due to self-steepening over this propagation distance (a shift of the pulse peak by about 10fs) and exhibit none of the complex dynamics seen in Fig. 8. We therefore conclude that the simultaneous spatial and temporal collapse of the pulse observed here is a pure multimode effect, driven by FWM-based power exchange together with modal dispersion and self-steepening, in agreement with investigations based on beam propagation methods (Zharova et al., 2006).

## 5. Multimode effects in gas-filled waveguides

As discussed above, the peak power that can be transmitted in optical fibres is limited by the critical power for self-focusing and catastrophic collapse to levels of a few MW. According to Eq. (9), for a fixed laser wavelength $P_{crit}$ only depends on the material linear and nonlinear refractive index. In general, the linear refractive index does not vary much across transparent media, between 1 for vacuum and $\sim$4 for some non-silica glasses (Price et al., 2007) and semiconductors, whereas the nonlinear index $n_2$ can span many orders of magnitude. A common method for guiding extremely high power pulses is thus in hollow-core capillaries or fibres, where most of the light propagates in a gas. For example, $n_2 \approx 5 \times 10^{-23}$ m$^2$/W in air, compared to $2.5 \times 10^{-20}$ m$^2$/W in silica glass, thus pushing $P_{crit}$ into the GW regime. In contrast to solid-core fibres, gas-filled capillaries do not support strictly bound modes, but all modes are intrinsically leaky with losses scaling proportional to $\lambda^2/R^3$ where $\lambda$ is the light wavelength and $R$ is the radius of the capillary hole (Marcatili & Schmeltzer, 1964). Hence, the capillary hole must be sufficiently large in order to allow for transmission of light over long distances. For example, 800nm wavelength light propagating in the fundamental $LP_{01}$ mode of a silica glass capillary with a 75$\mu$m radius hole experiences losses of $\sim$3dB/m. For such a large hole compared to the laser wavelength, the capillary is multimoded, and this is the situation we will consider in the following. It should be noted, however, that single-mode guidance in hollow-core fibres is in principle possible using bandgap effects in photonic crystal fibres (Knight et al., 1998; Petrovich et al., 2008).

Using fs pulses at 800nm wavelength from commercial Ti:sapphire laser systems it is possible to reach peak powers large enough to observe nonlinear effects, and even self-focusing, in gases. Capillary guidance is used in this context for several high-power applications. One of these is pulse compression, where the nonlinearity of the gas in the capillary is exploited to spectrally broaden a pulse by self-phase modulation, which allows the pulse to be compressed after the capillary by purely dispersive means such as gratings or dispersive mirrors (Sartania et al., 1997). For intensities above $\sim 10^{13}\mathrm{W/cm}^2$, the electric field of the laser is large enough to start ionising the gaseous medium. The generated plasma exhibits a negative refractive index, which can counteract the self-focusing effect of the neutral gas and lead to pulse filamentation (Couairon & Mysyrowicz, 2007). In another application, ionisation and recombination effects are used for high harmonic generation of XUV and soft X-ray radiation, processes whose efficiencies can be enhanced significantly by phase matching techniques in capillaries (Rundquist et al., 1998).
In the following we will therefore discuss how the MM-NLSE can be extended to include these important effects and demonstrate a few sample effects related to the multimode nature of hollow capillaries typically used for such high-power applications.

### 5.1 Ionisation and plasma effects in the multimode nonlinear Schrödinger equation

The starting point for this derivation is the capability of high-intensity light to ionise the gas inside the capillary. Two effects contribute to the ionisation: (i) direct multiphoton ionisation, where several photons are absorbed simultaneously to eject one electron from its orbit, and (ii) tunneling ionisation, where the electric field of the laser is so strong that it deforms the electric potential of the nucleus and allows an electron to tunnel through the potential barrier. Tunneling ionisation occurs at higher field strengths than multiphoton ionisation, and is the dominant process for the effects we want to discuss here. The rate of tunneling ionisation $W$ can be calculated using Keldysh theory (Popov, 2004) as

$$W(\mathbf{x},t) = W_0 \kappa^2 \sqrt{\frac{3}{\pi}} C_{\kappa l}^2 2^{2n^*} F(\mathbf{x},t)^{1.5-2n^*} \exp\left(-\frac{2}{3F(\mathbf{x},t)}\right), \tag{12}$$

where $\kappa^2 = I_p/I_H$ is the ratio of the ionisation potential $I_p$ of the gas species over the ionisation potential for hydrogen $I_H = 13.6\mathrm{eV}$, $W_0 = m_e e^4/\hbar^3 = 4.13 \times 10^{16}\mathrm{s}^{-1}$, $F(\mathbf{x},t) = E'(\mathbf{x},t)/(\kappa^3 E_a)$ is the reduced electric field of the laser with $E_a = 5.14 \times 10^{11}\mathrm{V/m}$ the atomic unit of field intensity and $E'(\mathbf{x},t)$ the real-valued electric field in units of V/m corresponding to $\mathbf{E}(\mathbf{x},t)$, Eq. (1). The dimensionless parameters $C_{\kappa l}$ and $n^*$ are specific for the gas and can be looked up in tables (Popov, 2004). For the case of argon, which we will use as our example here, we have $I_p = 15.76\mathrm{eV}$, $C_{\kappa l} = 0.95$, and $n^* = 0.929$.
Given the modal amplitudes $A_p(z,t)$ we can calculate the electric field $\mathbf{E}(\mathbf{x},t)$ and thus the ionisation rate $W(\mathbf{x},t)$ at every point and time in the capillary. From this we obtain the fraction of neutral atoms $r_0(\mathbf{x},t)$ and the fraction of ionised atoms $r_1(\mathbf{x},t) = 1 - r_0(\mathbf{x},t)$ by solving

$$\frac{\partial r_0(\mathbf{x},t)}{\partial t} = -W(\mathbf{x},t) r_0(\mathbf{x},t). \tag{13}$$

The generated plasma modifies the refractive index of the gas to

$$n(\mathbf{x},t) = \sqrt{1 - \frac{\omega_{pl}(\mathbf{x},t)^2}{\omega^2}}, \tag{14}$$

where the plasma frequency is given by

$$\omega_{pl}(\mathbf{x},t) = \sqrt{\frac{\rho r_1(\mathbf{x},t)e^2}{m_e \epsilon_0}}. \tag{15}$$

Here $\rho$ is the gas density and $e$ and $m_e$ are the electron charge and mass, respectively. The MM-NLSE thus aquires a new nonlinear term $\partial A_p(z,t)/\partial z \propto \mathcal{N}_{pl}\{A_p\}$ with

$$\mathcal{N}_{pl}\{A_p\} = -\left(1 - \frac{i}{\omega_0}\frac{\partial}{\partial t}\right)\frac{i}{2}k_0 \int \mathrm{d}x\mathrm{d}y \frac{\mathbf{F}_p(x,y)^* \cdot \mathbf{E}(\mathbf{x},t)}{\left[\int \mathrm{d}x\,\mathrm{d}y\,|\mathbf{F}_p|^2\right]^{1/2}} \frac{\omega_{pl}(\mathbf{x},t)^2}{\omega_0^2}, \tag{16}$$

which includes a self-steepening correction term and the projection of the modified laser field onto mode $p$ via a spatial overlap integral.
In addition to the effect of the plasma induced refractive index, we also have to consider the loss of energy from the propagating laser pulse due the ionisation process itself (Courtois et al., 2001). In the modal decomposition, this leads to a nonlinear loss term in the propagation of the mode envelope $A_p$ of the form

$$\mathcal{L}_{ion}\{A_p\} = -\frac{1}{2}\int \mathrm{d}x\mathrm{d}y \frac{\mathbf{F}_p(x,y)^* \cdot \mathbf{E}(\mathbf{x},t)}{\left[\int \mathrm{d}x\,\mathrm{d}y\,|\mathbf{F}_p|^2\right]^{1/2}} \frac{\rho r_0(\mathbf{x},t) W(\mathbf{x},t) I_p}{|\mathbf{E}(\mathbf{x},t)|^2}. \tag{17}$$

The full MM-NLSE in the presence of gas ionisation by tunneling in the strong-field limit thus becomes (Chapman et al., 2010)

$$\frac{\partial A_p}{\partial z} = \mathcal{D}\{A_p\} + \mathcal{N}\{A_p\} + \mathcal{N}_{pl}\{A_p\} + \mathcal{L}_{ion}\{A_p\} \tag{18}$$

where the individual terms are given by (2), (3), (16) and (17).

### 5.2 Ultrashort pulse propagation in capillaries

In the following we present simulation results of the extended MM-NLSE (18) for a specific experimental situation (Froud et al., 2009). In particular, we consider a 7cm long capillary with a 75$\mu$m radius hole filled with argon at a pressure of 80mbar in the central 3cm of the capillary; the Ar pressure tapers down over 2cm to 0mbar at the input and output. Laser pulses of 40fs length at 780nm wavelength are launched with a Gaussian waist of 40$\mu$m centred into the capillary. For the simulations, 20 linearly polarised $LP_{0n}$ modes are considered, as discussed in Sec. 2.2.
Results from two sets of simulations with different launched pulse energies, 0.5mJ and 0.7mJ, respectively, are presented in Fig. 9. The distribution of $Ar^+$ ions in the capillary is shown in Figs. 9(a) and (b). As expected, ionisation mainly occurs on axis where the laser intensity is maximum. Moreover, because the transverse beam size of the launched laser pulses is not ideally matched to the fundamental mode of the capillary, power is also coupled into the first higher order mode, which leads to mode beating and thus to the periodic ionisation pattern along the capillary length with a periodicity of ~2cm, observed most clearly at lower powers, Fig. 9(a). At higher powers, the nonlinear ionisation processes become much stronger and a spate of additional radial and longitudinal structures are found in the ionisation pattern, Fig. 9(b). In Fig. 9(c) the partial $Ar^+$ pressures of (a) and (b) are averaged over the transverse cross section of the capillary. The distribution shown in this figure can be easily verified

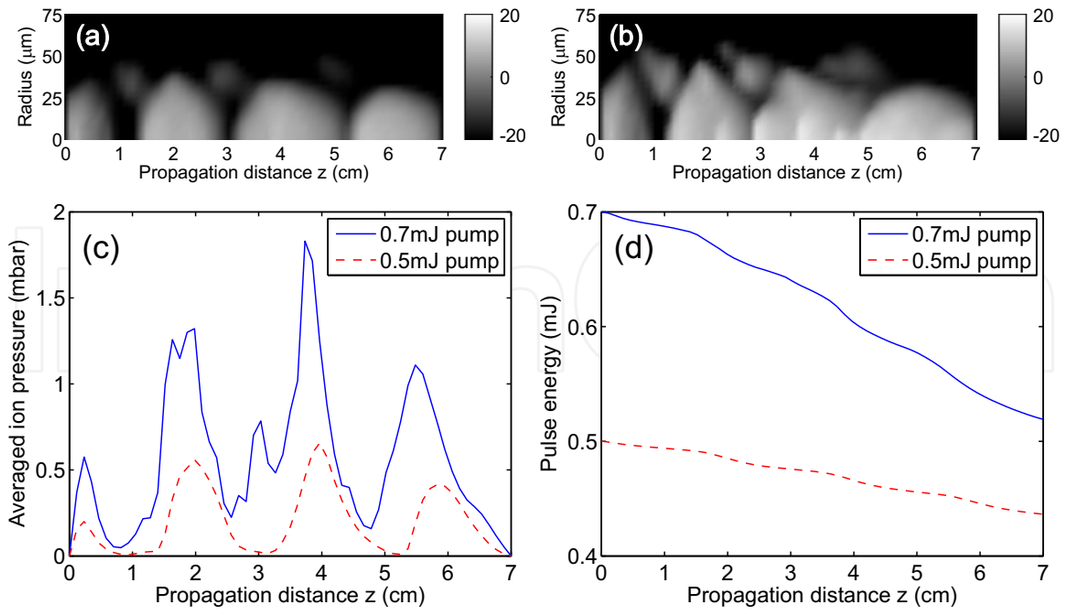


Fig. 9. Propagation of 40fs pulses at 780nm wavelength in a hollow-core capillary (length 7cm, hole radius 75$\mu$m) filled with argon with partial ionisation. (a), (b) Partial pressure of $Ar^+$ ions (in dB of mbar) vs position $z$ and radius $r$ inside the capillary for launched pulse energies of 0.5mJ and 0.7mJ, respectively. (c) $Ar^+$ pressure averaged over the capillary cross section vs $z$. (d) Corresponding integrated pulse energy vs $z$. The total gas pressure in the capillary centre is 80mbar.

experimentally as it is proportional to the intensity of the $Ar^+$ ion fluorescence observed at 488nm (Chapman et al., 2010; Froud et al., 2009). Finally, in Fig. 9(d) the pulse energy summed over all modes is presented versus the propagation distance for these two simulations. The effect of propagation losses due to ionisation, described by the term $\mathcal{L}_{ion}\{A_p\}$ in Eq. (17), is clearly visible with strong losses associated with the peaks of large ionisation in Fig. 9(c). Because of the highly nonlinear nature of tunneling ionisation, losses at slightly higher input energies (0.7mJ instead of 0.5mJ) are several times larger.

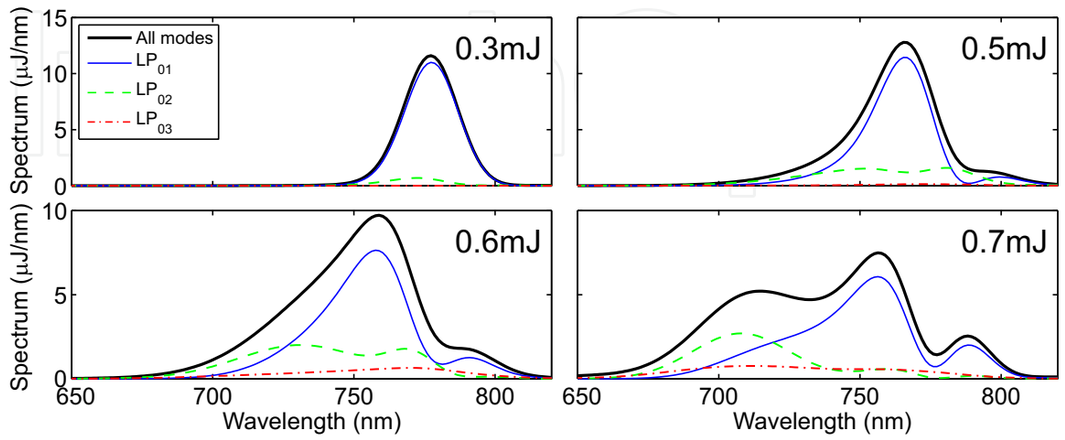


Fig. 10. Pulse spectra and modal contributions at the capillary output for launched pulse energies in the range 0.3mJ to 0.7mJ. Other parameters as in Fig. 9.

The spatial and temporal distribution of ions generated by the propagating laser pulse acts back on the pulse through its (negative) refractive index, according to the term $\mathcal{N}_{pl}\{A_p\}$ given in Eq. (16). Because of the strong localisation of the regions with high ionisation, different capillary modes are affected differently resulting in strong intermodal scattering and mode-specific spectral broadening, as is demonstrated in Fig. 10. At a relatively low pulse energy of 0.3mJ where ionisation is weak, a slight blue-shift of the spectral contribution of the excited $LP_{02}$ mode is observed, but no higher order mode excitation. Increasing the pulse energy to 0.5-0.7mJ, more and more light is scattered into higher order modes. Moreover, the spectrum first develops a small peak at the long-wavelength side of the pump (790-800nm) and then a very broad and high-intensity shoulder at short wavelengths. It is interesting to note that these short wavelength parts of the spectrum are more pronounced in the higher order modes $LP_{02}$ and $LP_{03}$ of the capillary, in fact they contain more power than the fundamental mode at these wavelengths for launched pulse energies above 0.6mJ. This finding has again been confirmed by experiments, where a strong position-dependence of the spectrum was observed in the far field beyond the capillary (Chapman et al., 2010).
These selected results demonstrate clearly that mode interference and mode coupling, i.e., transverse spatial effects, play a significant role in the propagation of high-intensity laser pulses in regimes where ionisation becomes important. This also impacts other applications of such systems, for example the angular dependence of high harmonic generation as recently observed in a capillary-based XUV source (Praeger et al., 2007).

## 6. Conclusions and outlook

To summarise, we presented an analysis of nonlinear effects of short laser pulses propagating in multimode optical fibres. We developed a general theoretical framework which is based on the modal decomposition of the propagating light and takes the form of a multimode generalised nonlinear Schrödinger equation. This approach provides new insights into the significance of fibre properties, e.g., modal dispersion and mode overlaps, for nonlinear pulse propagation, and for moderately multimode fibres and waveguides it has been shown to be numerically significantly more efficient than beam propagation methods. We subsequently discussed several applications of the model covering laser peak powers in the kW (supercontinuum generation), MW (self-focusing effects) and GW regime (ionisation and plasma nonlinearities) highlighting the importance of multimode effects throughout.
While we focused our discussion here on the high-power regime, we emphasise that there is also rapidly growing interest in the application of multimode fibres at low, W-level peak powers. A fast emerging area of interest comes, for example, from optical telecommunications, where in an attempt to increase the fibre capacity researchers are now considering the use of several fibre modes, or several cores within a single fibre, as independent channels. Intermodal nonlinear effects are expected to pose an ultimate limit to the maximum information capacity of the link, which we believe could be estimated by simulations using our model. Various sensing and imaging applications can also benefit from multimode fibres. Moreover, new sources in the mid-IR spectral region are currently being developed for spectroscopy and sensing applications that require novel waveguides such as soft glass fibres or semiconductor-based waveguides and fibres, some of which are intrinsically multimoded at near-IR pump wavelengths. We therefore expect that the multimode nonlinear Schrödinger equation discussed in this work will provide a valuable tool in the analysis and investigation of many future photonics applications.

## 7. Acknowledgements

The authors acknowledge financial support by the U.K. Engineering and Physical Sciences Research Council (EPSRC) and the Royal Society. We thank Prof. D. J. Richardson, Dr. W. S. Brocklesby, and Prof. J. G. Frey for valuable discussions.

## 8. References

Agrawal, G. P. (2001). *Nonlinear Fiber Optics*, 3rd ed., Academic Press, San Diego, USA.

Askaryan, G. A. (1962). Effects of the gradient of strong electromagnetic beam on electrons and atoms, *Sov. Phys. JETP*, Vol. 15, 1088–1090.

Blow, K. J., & Wood, D. (1989). Theoretical description of transient stimulated Raman scattering in optical fibers. *IEEE J. Quantum Electron.*, Vol. 25, No. 12, 2665–2673.

Brabec, T., & Krausz, F. (1997). Nonlinear optical pulse propagation in the single-cycle regime. *Phys. Rev. Lett.*, Vol. 78, No. 17, 3282–3285.

Chaipiboonwong, T., Horak, P., Mills, J. D., & Brocklesby, W. S. (2007). Numerical study of nonlinear interactions in a multimode waveguide. *Opt. Expr.*, Vol. 15, 9040–9047.

Chapman, R. T., Butcher, T. J., Horak, P., Poletti, F., Frey, J. G., & Brocklesby, W. S. (2010). Modal effects on pump-pulse propagation in an Ar-filled capillary. *Opt. Expr.*, Vol. 18, No. 12, 13279–13284.

Chiao, R. Y., Garmire, E., & Townes, C. H. (1964). Self-trapping of optical beams. *Phys. Rev. Lett.*, Vol. 13, No. 15, 479–482.

Coen, S., Chau, A. H. L., Leonhardt, R., Harvey, J. D., Knight, J. C., Wadsworth, W. J., & Russell, P. St. J. (2002). Supercontinuum generation by stimulated Raman scattering and parametric four-wave mixing in photonic crystal fibers. *J. Opt. Soc. Am. B*, Vol. 19, No. 4, 753–764.

Couairon, A., & Mysyrowicz, A. (2007). Femtosecond filamentation in transparent media. *Phys. Rep.*, Vol. 441, 47–189.

Courtois, C., Couairon, A., Cros, B., Marquès, J. R., & Matthieussent, G. (2001). Propagation of intense ultrashort laser pulses in a plasma filled capillary tube: Simulations and experiments. *Phys. Plas.*, Vol. 8, No. 7, 3445–3456.

Delmonte, T., Watson, M. A., O'Driscoll, E. J., Feng, X., Monro, T. M., Finazzi, V., Petropoulos, P., Price, J. H. V., Baggett, J. C., Loh, W., Richardson, D. J., & Hand, D. P. (2006). Generation of mid-IR continuum using tellurite microstructured fiber. *Conference on Lasers and Electro-Optics*, paper CTuA4, Long Beach, USA.

Dudley, J. M., Provino, L., Grossard, N., Maillotte, H., Windeler, R. S., Eggleton, B. J., & Coen, S. (2002). Supercontinuum generation in air-silica microstructured fibers with nanosecond and femtosecond pulse pumping. *J. Opt. Soc. Am. B*, Vol. 19, No. 4, 765–771.

Dudley, J. M., Genty, G., & Coen, S. (2006). Supercontinuum generation in photonic crystal fiber. *Rev. Mod. Phys.*, Vol. 78, No. 4, 1135–1184.

Dupriez, P., Poletti, F., Horak, P., Petrovich, M. N., Jeong, Y., Nilsson, J., Richardson, D. J., & Payne, D. N. (2007). Efficient white light generation in secondary cores of holey fibers. *Opt. Expr.*, Vol. 15, No. 7, 3729–3736.

Farrow, R. L., Kliner, D. A. V., Hadley, G. R., & Smith, A. V. (2006). Peak-power limits on fiber amplifiers imposed by self-focusing. *Opt. Lett.*, Vol. 31, No. 23, 3423–3425.

Fibich, G., & Gaeta, A. (2000). Critical power for self-focusing in bulk media and in hollow waveguides. *Opt. Lett.*, Vol. 25, No. 5, 335–337.

Froud, C. A., Chapman, R. T., Rogers, E. T. F., Praeger, M., Mills, B., Grant-Jacob, J., Butcher, T. J. , Stebbings, S. L., de Paula, A. M., Frey, J. G., & Brocklesby, W. S. (2009). Spatially resolved $Ar^{*}$ and $Ar^{+*}$ imaging as a diagnostic for capillary-based high harmonic generation. *J. Opt. A*, Vol. 11, 054011.

Gaeta, A. (2000). Catastrophic collapse of ultrashort pulses. *Phys. Rev. Lett.*, Vol. 84, No. 16, 3582–3585.

Galvanauskas, A., Cheng, M.-Y., Hou, K.-C., Liao, K.-H. (2007). High peak power pulse amplification in large-core Yb-doped fiber amplifiers. *IEEE J. Sel. Top. Quantum Electron.*, Vol. 13, No. 3, 559–566.

Hasegawa, A., & Tappert, F. (1973). Transmission of stationary nonlinear optical pulses in dispersive dielectric fibers. I. Anomalous dispersion. *Appl. Phys. Lett.*, Vol. 23, No. 3, 142–144.

Horak, P., & Poletti, F. (2009). Effects of pulse self-focusing on supercontinuum generation in multimode optical fibers. *International Conference on Transparent Optical Networks*, Ponta Delgada, Portugal, 28 June - 2 July 2009.

Jeong, Y., Sahu, J. K., Payne, D. N., & Nilsson, J. (2004). Ytterbium-doped large-core fiber laser with 1.36 kW continuous-wave output power. *Opt. Expr.*, Vol. 12, No. 25, 6088–6092.

Kao, K. C., & Hockham, G. A. (1966). Dielectric-fibre surface waveguides for optical frequencies. *Proc. IEE*, Vol. 113, No. 7, 1151–1158.

Knight, J. C., Broeng, J., Birks, T. A., & Russell, P. St. J. (1998). Photonic band gap guidance in optical fibers. *Science*, Vol. 282, 1476–1478.

Lehtonen, M., Genty, G., Ludvigsen, H., & Kaivola, M. (2003). Supercontinuum generation in a highly birefringent microstructured fiber. *Appl. Phys. Lett.*, Vol. 82, No. 14, 2197–2199.

Lesvigne, C., Couderc, V., Tonello, A., Leproux, P., Barthelemy, A., Lacroix, S., Druon, F., Blandin, P., Hanna, M., & Georges, P. (2007). Visible supercontinuum generation controlled by intermodal four-wave mixing in microstructured fiber. *Opt. Lett.*, Vol. 32, No. 15, 2173–2175.

Marcatili, E. A. J., & Schmeltzer, R. A. (1964). Hollow metallic and dielectric waveguides for long distance optical transmission and lasers. *Bell Tech. Syst. J.*, Vol. 43, 1783–1809.

Martins, E. R., Spadoti, D. H., Romero, M. A., & Borges, B.-H. V. (2007). Theoretical analysis of supercontinuum generation in a highly birefringent D-shaped microstructured optical fiber. *Opt. Expr.*, Vol. 15, No. 22, 14335–14347.

Mears, R. J., Reekie, L., Jauncey, I. M., & Payne, D. N. (1987). Low-noise Erbium-doped fiber amplifier at 1.54$\mu$m. *Electron. Lett.*, Vol. 23, No. 19, 1026–1028.

Milosevic, N., Tempea, G., & Brabec, T. (2000). Optical pulse compression: bulk media versus hollow waveguides. *Opt. Lett.*, Vol. 25, No. 9, 672–674.

Miya, T., Terunuma, Y., Hosaka, T., & Miyashita, T. (1979). Ultimate low-loss single-mode fibre at 1.55$\mu$m. *Electron. Lett.*, Vol. 15, No. 4, 106–108.

Mortensen, N. A., Nielsen, M. D., Folkenberg, J. R., Petersson, A., & Simonsen, H. R. (2003). Improved large-mode-area endlessly single-mode photonic crystal fibers. *Opt. Lett.*, Vol. 28, No. 6, 393–395.

Okamoto, K. (2006). *Fundamentals of Optical Waveguides*, 2nd ed., Academic Press, San Diego, USA.

Petrovich, M. N., Poletti, F., van Brakel, A., & Richardson, D. J. (2008). Robustly single mode hollow core photonic bandgap fiber. *Opt. Expr.*, Vol. 16, No. 6, 4337–4346.

Poletti, F., & Horak, P. (2008). Description of ultrashort pulse propagation in multimode optical fibers. *J. Opt. Soc. Am. B*, Vol. 25, No. 10, 1645–1654.

Poletti, F., & Horak, P. (2009). Dynamics of femtosecond supercontinuum generation in multimode fibers. *Opt. Expr.*, Vol. 17, No. 8, 6134–6147.

Popov, V. S. (2004). Tunnel and multiphoton ionization of atoms and ions in a strong laser field (Keldysh theory). *Physics-Uspekhi*, Vol. 47, No. 9, 855–885.

Praeger, M., de Paula, A. M., Froud, C. A., Rogers, E. T. F., Stebbings, S. L., Brocklesby, W. S., Baumberg, J. J., Hanna, D. C., & Frey, J. G. (2007). Spatially resolved soft X-ray spectrometry from single-image diffraction. *Nat. Phys.*, Vol. 3, 176–179.

Press, W. H., Teukolsky, S. A., Vetterling, W. T., & Flannery, B. P. *Numerical recipes: the art of scientific computing*, 3rd ed. (Cambridge University Press, New York, USA, 2007).

Price, J. H. V., Monro, T. M., Furusawa, K., Belardi, W., Baggett, J. C., Coyle, S., Netti, C., Baumberg, J. J., Paschotta, R., & Richardson, D. J. (2003). UV generation in a pure-silica holey fiber. *Appl. Phys. B*, Vol. 77, No. 2–3, 291–298.

Price, J. H. V., Monro, T. M., Ebendorff-Heidepriem, H., Poletti, F., Horak, P., Finazzi, V., Leong, J. Y. Y., Petropoulos, P., Flanagan, J. C., Brambilla, G., Feng, X., & Richardson, D. J. (2007). Mid-IR supercontinuum generation from nonsilica microstructured optical fibers. *J. Sel. Top. Quantum Electron.*, Vol. 13, No. 3, 738–749.

Ranka, J. K., & Gaeta, A. L. (2009). Breakdown of the slowly varying envelope approximation in the self-focusing of ultrashort pulses. *Opt. Lett.*, Vol. 23, No. 7, 534–536.

Roppo, V., Centini, M., Sibilia, C., Bertolotti, M., de Ceglia, D., Scalora, M., Akozbek, N., Bloemer, M. J., Haus, J. W., Kosareva, O. G., & Kandidov, V. P. (2007). Role of phase matching in pulsed second-harmonic generation: Walk-off and phase-locked twin pulses in negative-index media. *Phys. Rev. A*, Vol. 76, No. 3, 033829.

Rundquist, A., Durfee, C. G., Chang, Z., Herne, C., Backus, S., Murnane, M. M., & Kapteyn, H. C. (1998). Phase-matched generation of coherent soft X-rays. *Science*, Vol. 280, 1412–1415.

Sartania, S., Cheng, Z., Lenzner, M., Tempea, G., Spielmann, Ch., Krausz, F., and Ferencz, K. (1997). Generation of 0.1-TW 5-fs optical pulses at a 1-kHz repetition rate. *Opt. Lett.*, Vol. 22, No. 20, 1562–1564.

Schreiber, T., Andersen, T., Schimpf, D., Limpert, J., & Tünnermann, A. (2005). Supercontinuum generation by femtosecond single and dual wavelength pumping in photonic crystal fibers with two zero dispersion wavelengths. *Opt. Expr.*, Vol. 13, No. 23, 9556–9569.

Stolen, R. H., Ippen, E. P., & Tynes, A. R. (1972). Raman oscillation in glass optical waveguide. *Appl. Phys. Lett.*, Vol. 20, No. 2, 62–64.

Stolen, R. H., & Bjorkholm, J. B. (1982). Parametric amplification and frequency conversion in optical fibers. *IEEE J. Quantum Electron.*, Vol. 18, No. 7, 1062–1072.

Stuart, B. C., Feit, M. D., Herman, S., Rubenchik, A. M., Shore, B. W., & Perry, M. D. (1996). Nanosecond-to-femtosectond laser-induced breakdown in dielectrics. *Phys. Rev. B*, Vol. 53, No. 4, 1749–1761.

Tonello, A., Pitois, S., Wabnitz, S., Millot, G., Martynkien, T., Urbanczyk, W., Wojcik, J., Locatelli, A., Conforti, M., & De Angelis, C. (2006). Frequency tunable polarization and intermodal modulation instability in high birefringence holey fiber. *Opt. Expr.*, Vol. 14, No. 1, 397–404.

Zharova, N. A., Litvak, A. G., & Mironov, V. A. (2006). Self-focusing of wave packets and envelope shock formation in nonlinear dispersive media. *J. Exp. Theor. Phys.*, Vol. 103, No. 1, 15–22.


**Recent Progress in Optical Fiber Research**

Edited by Dr Moh. Yasin

ISBN 978-953-307-823-6

Hard cover, 450 pages

**Publisher** InTech

**Published online** 25, January, 2012

**Published in print edition** January, 2012

This book presents a comprehensive account of the recent progress in optical fiber research. It consists of four sections with 20 chapters covering the topics of nonlinear and polarisation effects in optical fibers, photonic crystal fibers and new applications for optical fibers. Section 1 reviews nonlinear effects in optical fibers in terms of theoretical analysis, experiments and applications. Section 2 presents polarization mode dispersion, chromatic dispersion and polarization dependent losses in optical fibers, fiber birefringence effects and spun fibers. Section 3 and 4 cover the topics of photonic crystal fibers and a new trend of optical fiber applications. Edited by three scientists with wide knowledge and experience in the field of fiber optics and photonics, the book brings together leading academics and practitioners in a comprehensive and incisive treatment of the subject. This is an essential point of reference for researchers working and teaching in optical fiber technologies, and for industrial users who need to be aware of current developments in optical fiber research areas.



**InTech Europe**
University Campus STeP Ri
Slavka Krautzeka 83/A
51000 Rijeka, Croatia
Phone: +385 (51) 770 447
Fax: +385 (51) 686 166
www.intechopen.com

**InTech China**
Unit 405, Office Block, Hotel Equatorial Shanghai
No.65, Yan An Road (West), Shanghai, 200040, China
中国上海市延安西路65号上海国际贵都大饭店办公楼405单元
Phone: +86-21-62489820
Fax: +86-21-62489821

IntechOpen